Journal of Physical Science
Vol. 37(1), 63–76, 2026

Structural Characteristics of $Sn(Se_xTe_{1-x})$ Thin Films Fabricated from Bulk Alloys via Vacuum Evaporation

Riza Ariyani Nur Khasanah,[1,2*] Rita Prasetyowati[1,2] and Ariswan[1,2*]

[1]Department of Physics Education, Universitas Negeri Yogyakarta, 55281 Yogyakarta, Indonesia
[2]Nanotechnology for Advanced Waste Management and Sustainable Environment Optimization, Universitas Negeri Yogyakarta, 55281 Yogyakarta, Indonesia

Corresponding author: rizaariyani@uny.ac.id, ariswan@uny.ac.id

Published online: 29 April 2026

To cite this article: Khasanah, R. A. N. et al. (2026). Structural characteristics of $Sn(Se_xTe_{1-x})$ thin films fabricated from bulk alloys via vacuum evaporation. *J. Phys. Sci.*, 37(1), 63–76. https://doi.org/10.21315/jps2026.37.1.4

To link this article: https://doi.org/10.21315/jps2026.37.1.4

ABSTRACT: Tin selenide-telluride ($Sn[Se_xTe_{1-x}]$) alloys are promising candidates for next-generation solar cell applications; however, their structural characteristics are still not fully understood. This study investigates the effect of selenium (Se) and tellurium (Te) composition on the structural properties of bulk-derived $Sn(Se_xTe_{1-x})$ thin films with x = 0.0, 0.2, 0.4, 0.6, 0.8 and 1.0. The bulk alloys were synthesised using the Bridgman method and subsequently employed as source materials for the thin-film fabrication via vacuum evaporation. Energy-dispersive X-ray spectroscopy analysis revealed increasing deviations from ideal stoichiometry with higher Se content, particularly in the bulk samples. In contrast, the thin films exhibited compositions closer to the intended Se-to-Te ratios, attributed to more controlled deposition and reduced segregation during film growth. Scanning electron microscopy analysis showed that bulk samples exhibited significant grain structure variation with increasing Se content, whereas thin films displayed a more uniform morphology—transitioning from granular to nanostructured features. X-ray diffraction analysis revealed a structural transition from a cubic phase (SnTe, x = 0.0) to an orthorhombic phase at higher Se concentrations ($x \geq 0.6$), accompanied by corresponding changes in lattice parameters. At x = 1.0 (SnSe), both the bulk and thin-film samples exhibited identical lattice parameters (a = 11.470 Å, b = 4.152 Å and c = 4.439 Å), confirming the formation of a pure orthorhombic phase. These findings emphasise the importance of compositional control in tuning the structural phases of $Sn(Se_xTe_{1-x})$ alloys and demonstrate the viability of fabricating high-quality thin films from bulk-derived source materials. The successful transfer of structural integrity from bulk to thin-film form opens new avenues for optimising these materials for photovoltaic device applications.

Keywords: $Sn(Se_xTe_{1-x})$ alloys, bulk, thin films, structural transition, vacuum evaporation

1. INTRODUCTION

The ongoing development of renewable energy is crucial for mitigating the global energy crisis. Among various approaches, harnessing solar energy—our most abundant energy source—has gained significant attention. Researchers have focused on advancements in photovoltaic technology and photocatalysis to efficiently convert solar energy into usable forms.[1–3] Photovoltaic technology, commonly referred to as solar cells, utilises semiconductor materials to convert solar energy into electrical energy owing to their ability to absorb light and facilitate charge transport.[4] The efficiency and performance of these cells depend significantly on the properties of the semiconductor materials.[1,5–7]

Among various semiconductor materials, tin chalcogenide semiconductor alloys, such as tin selenide (SnSe) and tin telluride (SnTe), are particularly promising for solar cell applications due to their efficient light absorption and excellent electrical conductivity.[8–10] These materials also offer the advantages of being low-cost and non-toxic.[11] SnSe, a p-type semiconductor, has an energy gap of approximately 0.9 eV–1.3 eV, making it suitable for photovoltaic applications with an efficiency of about 23% as well as for photodetectors.[12–14] SnSe exhibits an orthorhombic structure with a space group of *Pnma*.[15] The crystal phase of SnSe has attracted great interest for photovoltaic cells because it represents an intermediate between three-dimensional crystalline networks and two-dimensional layered compounds.[16] On the other hand, SnTe is a narrow band gap semiconductor (approximately 0.1 eV–0.25 eV) and is primarily used as a thermoelectric material.[17] The crystal structure of SnTe exhibits a cubic structure with a space group of $Fm\bar{3}m$.[18,19] The formation of tin selenide-telluride ($Sn[Se_xTe_{1-x}]$) combines the favourable transport properties of SnTe with the wider band gap and structural stability of SnSe, enabling tuneable optoelectronic performance for solar cell applications. The crystal structure of solar cell semiconductors critically affects their band gap, carrier mobility and light absorption, determining overall efficiency.[20,21] Thus, achieving the appropriate crystal structure in $Sn(Se_xTe_{1-x})$ thin films is crucial for enhancing their photovoltaic performance.

In this study, $Sn(Se_xTe_{1-x})$ alloys with varying Se–Te compositions were first synthesised in bulk form using the Bridgman method and subsequently used as source materials to fabricate thin films via vacuum evaporation. Elemental composition analysis revealed stoichiometric deviations in both the bulk materials and thin films with increasing Se content, although the thin films exhibited a closer match to the ideal Se-to-Te ratio. A phase transition from a cubic structure at $x = 0.0$ to an orthorhombic structure at higher Se concentrations ($x \geq 0.6$) was observed in both bulk and thin-film forms, demonstrating the successful fabrication of thin films from bulk $Sn(Se_xTe_{1-x})$ alloys.

2. EXPERIMENTAL

2.1 Preparation of Bulk and Thin-Film $Sn(Se_xTe_{1-x})$ Alloys

The preparation of $Sn(Se_xTe_{1-x})$ alloys in both bulk and thin-film forms was carried out following established methodologies.[16,20] Bulk $Sn(Se_xTe_{1-x})$ alloys with varying Se and Te compositions (x = 0.0, 0.2, 0.4, 0.6, 0.8 and 1.0) were synthesised using high-purity Sn (99.99%), Se (99.99%) and Te (99.99%) via the Bridgman method. The composition parameter x for each alloy was carefully controlled, with the Se and Te fractions calculated accordingly. The mass of Se (m_{Se}) was determined using Equation (1), while the mass of Te (m_{Te}) was calculated using Equation (2).[16]

$$m_{Se} = \frac{m_{Sn}}{A_{Sn}}(x)\,A_{Se} \tag{1}$$

$$m_{Te} = \frac{m_{Sn}}{A_{Sn}}(1-x)\,A_{Te} \tag{2}$$

where m_{Sn} denotes the mass of Sn and A_{Se}, and A_{Te} represent the atomic weights of Se and Te, respectively. The constituent elements were mixed in a pyrex tube, previously cleaned using a solution of HF, HNO_3 and H_2O in a 2:3:5 ratio, then dried at 80°C for 8 h in a heating chamber. The tube was subsequently evacuated to 10^{-5} Torr, sealed by welding at one end, and the resulting capsule containing the Sn, Se and Te powders was subjected to controlled heating in a furnace.

The $Sn(Se_xTe_{1-x})$ thin films were fabricated using the vacuum evaporation technique. The substrates for the $Sn(Se_xTe_{1-x})$ thin films were glass slides with an area of 2 cm × 2 cm, and the coated area corresponded to the entire substrate surface. The source material was an Sn–Se–Te alloy initially synthesised via the Bridgman method, then ground into powder and placed in a molybdenum boat. A substrate heater was set to a temperature of 300°C or 350°C depending on the composition to promote effective thin-film crystallisation. These temperatures were selected based on optimisation trials in previous studies.[16,20] The deposition process was carried out under high-vacuum conditions, with a working pressure of approximately 4×10^{-5} Torr. Once a stable pressure was achieved, the source heater was set to 100 V, allowing the source material in the crucible to fully evaporate. The deposition time was approximately 5 min to ensure a uniform film thickness across all compositions. After deposition, the system was allowed to cool undisturbed for 12 h before the chamber was opened and the thin films were retrieved.

2.2 Characterisation of Bulk and Thin-Film $Sn(Se_xTe_{1-x})$ Alloys

The morphology and elemental composition of both the bulk materials and thin films of the $Sn(Se_xTe_{1-x})$ alloy were assessed using scanning electron microscopy (SEM, JSM-6360; JEOL Ltd., Tokyo, Japan), equipped with an energy-dispersive X-ray spectrometer (EDX). The EDX measurements were conducted on three different areas of each sample (both bulk and thin films), and the reported elemental compositions were the average values of these measurements to ensure representativeness. Crystal structure analysis was carried out using X-ray diffraction (XRD, MiniFlex 600, Rigaku Corp., Tokyo, Japan) with Cu Kα radiation (λ = 1.5406 Å). Instrument calibration and correction for displacement and zero shift were conducted using SRM Si640d.

3. RESULTS AND DISCUSSION

3.1 Elemental Composition

The elemental composition of both bulk materials and thin films of $Sn(Se_xTe_{1-x})$ alloy was investigated using EDX. Figure 1 presents the EDX spectra of the bulk alloys, with x = 0.2, 0.4, 0.6 and 0.8, while the EDX data for x = 0.0 and x = 1.0 have been reported in previous studies.[16,20] Table 1 summarises the elemental compositions of the bulk alloys, with an estimated EDX error of ± 1 at.%. The EDX analysis revealed deviations from the ideal stoichiometry in the bulk $Sn(Se_xTe_{1-x})$ alloys with increasing Se content. For x = 0.0, the measured composition was Sn = 53.60% and Te = 46.95%, with no detectable Se, corresponding to a formula of $SnTe0_{.88}$, indicating a slight deficiency in Te. As x increased, the measured Se content also rose, accompanied by a corresponding decrease in Te content. At x = 0.6, the deviation became more significant, with Se content reaching 30.52% and Te content decreasing to 10.89%, resulting in a formula of $Sn(Se_{0.52}Te_{0.2})$. For x = 1.0, the measured composition was $SnSe_{0.94}$, which closely approximates the expected stoichiometry of SnSe.

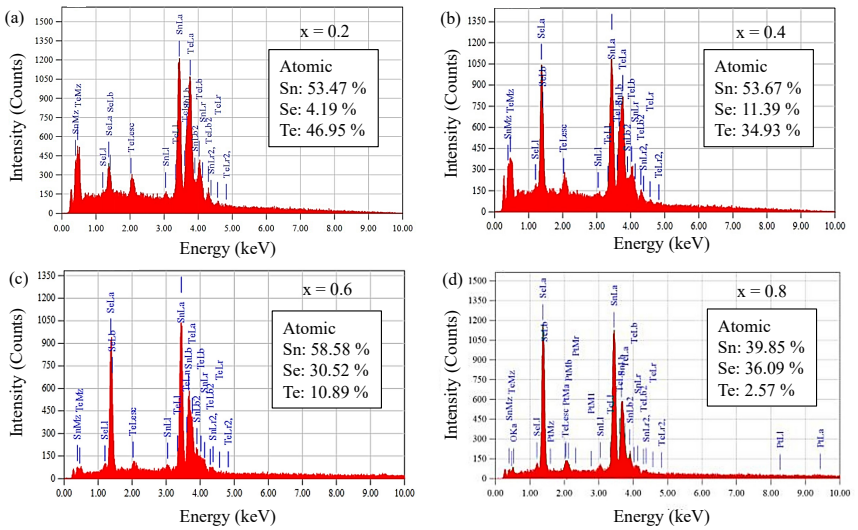

Figure 1: EDX spectra of $Sn(Se_xTe_{1-x})$ bulk alloys with varying Se content: (a) x = 0.2, (b) x = 0.4, (c) x = 0.6 and (d) x = 0.8.

Table 1: Elemental composition of $Sn(Se_xTe_{x-1})$ bulk alloys analysed by EDX

No	x	Ideal composition	Elemental composition from EDX (%)			Measured composition
			Sn	Se	Te	
1	0.0	SnTe	53.60	0	46.95	$SnTe_{0.88}$
2	0.2	$Sn(Se_{0.2}Te_{0.8})$	53.47	4.19	42.34	$Sn(Se_{0.1}Te_{0.8})$
3	0.4	$Sn(Se_{0.4}Te_{0.6})$	53.67	11.39	34.93	$Sn(Se_{0.2}Te_{0.6})$
4	0.6	$Sn(Se_{0.6}Te_{0.4})$	58.58	30.52	10.89	$Sn(Se_{0.52}Te_{0.2})$
5	0.8	$Sn(Se_{0.8}Te_{0.2})$	39.85	36.09	2.57	$Sn(Se_{0.9}Te_{0.1})$
6	1.0	SnSe	49.18	50.82	0	$SnSe_{0.94}$

The $Sn(Se_xTe_{1-x})$ thin films were synthesised using bulk alloys, which had been previously prepared and characterised. Given that the elemental compositions of the bulk materials deviated from the ideal stoichiometry, it is important to evaluate how these deviations influence the resulting thin films. To assess the elemental composition of the thin films, EDX measurements were conducted, as shown in Figure 2 for x = 0.2, 0.4, 0.6 and 0.8, while the compositions for x = 0.0 and x = 1.0 were reported in previous studies.[16,20] The corresponding quantitative data are summarised in Table 2. EDX analysis revealed that the actual compositions of the $Sn(Se_xTe_{1-x})$ thin films slightly deviated from the ideal stoichiometric values. In contrast to bulk alloys,

the measured compositions of the thin films were closer to the ideal, with formulas of $SnTe_{0.94}$, $Sn(Se_{0.2}Te_{0.7})$, $Sn(Se_{0.44}Te_{0.51})$, $Sn(Se_{0.55}Te_{0.38})$, $Sn(Se_{0.83}Te_{0.18})$ and $SnSe_{0.94}$ for x = 0.0, 0.2, 0.4, 0.6, 0.8 and 1.0, respectively. The thin films exhibited compositions that were more closely aligned with the ideal stoichiometry than their bulk counterparts, suggesting that the vacuum evaporation process allowed for better control over compositional accuracy, likely due to reduced segregation effects and more stable deposition conditions.[9,20–23] These differences may be attributed to factors such as the higher vapour pressure of Se compared to Te, substrate interactions and thermal re-evaporation during film growth.[20,21]

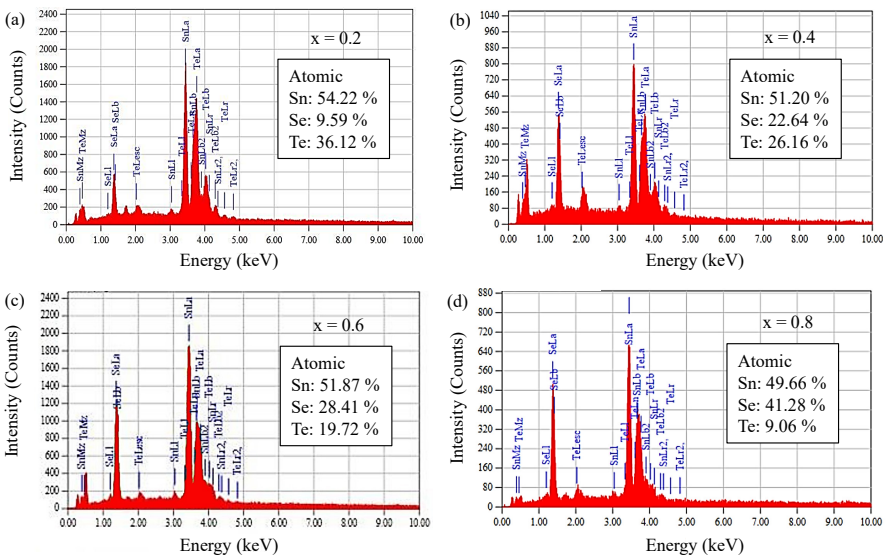

Figure 2: EDX spectra of bulk-derived $Sn(Se_xTe_{1-x})$ thin films with varying Se content: (a) x = 0.2, (b) x = 0.4, (c) x = 0.6 and (d) x = 0.8.

Table 2: Elemental composition of bulk-derived $Sn(Se_xTe_{x-1})$ thin films analysed by EDX

No	x	Ideal composition	Elemental composition from EDX (%)			Measured composition
			Sn	Se	Te	
1	0.0	SnTe	51.92	0	49.08	$SnTe_{0.94}$
2	0.2	$Sn(Se_{0.2}Te_{0.8})$	54.22	9.59	36.12	$Sn(Se_{0.2}Te_{0.7})$
3	0.4	$Sn(Se_{0.4}Te_{0.6})$	51.20	22.64	26.16	$Sn(Se_{0.44}Te_{0.51})$
4	0.6	$Sn(Se_{0.6}Te_{0.4})$	51.87	28.41	19.72	$Sn(Se_{0.55}Te_{0.38})$
5	0.8	$Sn(Se_{0.8}Te_{0.2})$	49.66	41.28	9.06	$Sn(Se_{0.83}Te_{0.18})$
6	1.0	SnSe	49.18	50.82	0	$SnSe_{0.94}$

3.2 Surface Morphology

The SEM images presented in Figure 3 provide a direct comparison of the morphological characteristics between bulk materials and thin films. The bulk samples displayed distinct grain structures. At x = 0.2, large-faceted grains were observed, characteristic of the slow solidification associated with the Bridgman method (Figure 3[a]). At x = 0.6, the grains appeared smaller and more aggregated, indicating a shift in nucleation and growth behaviour as the Se content increased (Figure 3[b]). In contrast, the thin-film samples exhibited a more uniform morphology. The sample with x = 0.2 showed a fine granular structure, suggesting a homogeneous film with limited grain coalescence (Figure 3[c]) . At x = 0.6 and x = 1.0, the surface evolved into a nanostructured pattern, likely influenced by deposition rate and substrate interaction (Figures 3[d] and 3[e]). The $Sn(Se_xTe_{1-x})$ thin films were deposited using identical vacuum evaporation parameters, resulting in comparable estimated thicknesses of approximately 1.5 µm, based on cross-sectional SEM analysis (Figure 3[f], SnSe sample).

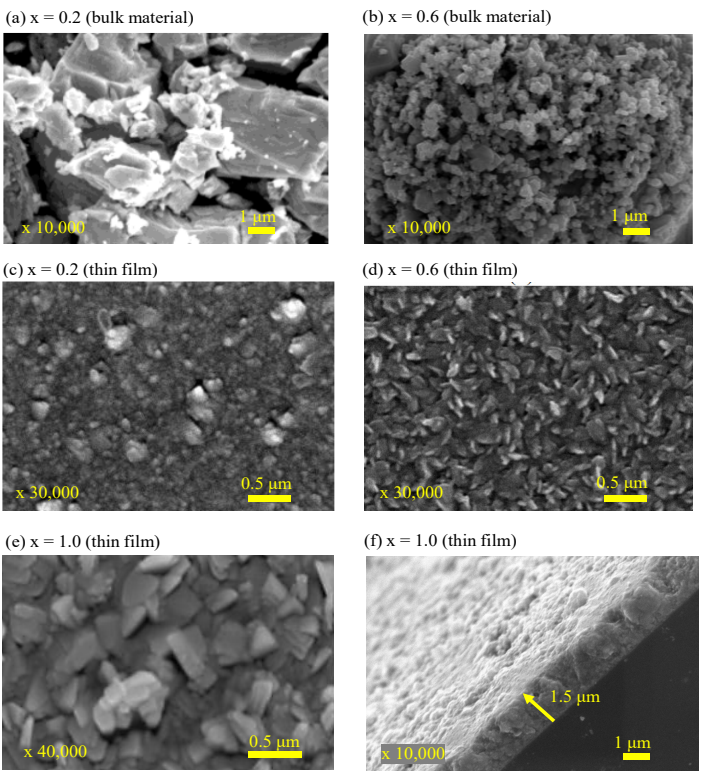

Figure 3: SEM images of $Sn(Se_xTe_{1-x})$ alloys: (a, b) bulk sample with x = 0.2 and 0.6; (c–e) thin films with x = 0.2, 0.6 and 1.0; (f) cross-sectional image of the SnSe thin-film.

Although this thickness is slightly above the typical submicron range, it remains consistent with previous reports (approximately 1.3 μm),[9] and is still commonly referred to as "thin-film" in photovoltaic research due to its uniform deposition on thick glass substrates.

3.3 Crystal Structure

Despite minor discrepancies, the elemental composition of both bulk and thin-film samples remained within acceptable ranges and was considered suitable for further structural analysis. The lattice parameters of $Sn(Se_xTe_{1-x})$ alloys in both bulk and thin-film forms were analysed based on their XRD patterns. Figure 4(a) presents the XRD results for bulk samples, with x = 0.0–1.0. At x = 0.0, the diffraction peaks observed at 2θ values of 28.30°, 40.46°, 50.10°, 58.50°, 66.18° and 73.65° were indexed to the (200), (220), (222), (400), (420) and (422) planes, respectively, in accordance with the JCPDS reference for cubic SnTe (No. 46-1210).[11,18] In contrast, for x = 1.0, the XRD patterns exhibited diffraction peaks at 2θ values of 30.06°, 30.70°, 37.47°, 43.60°, 49.42°, 51.49°, 54.14° and 64.70°, corresponding to the (011), (111), (311), (020), (302), (511), (420) and (800) planes, respectively. These peaks matched well with the JCPDS reference for orthorhombic SnSe (No. 32-1382).[12,18,24] For intermediate compositions (x = 0.2–0.8), the diffraction patterns indicated the coexistence of SnTe and SnSe phases. Notably, at x = 0.2 and 0.4, SnTe peaks were more dominant, although weak SnSe peaks could still be detected with (111) plane at 2θ ≈ 30.70°. The intensity ratio of the SnSe (111) peak to the SnTe (200) peak for x = 0.2 and 0.4 was approximately 0.5, indicating that the samples were still predominantly cubic. Moreover, at x = 0.5, the intensity ratio increased to 1.6, indicating a more balanced biphasic structure (Figure 4[b]). Conversely, at x = 0.6 and 0.8, the dominant peaks corresponded to SnSe, while weak SnTe peaks remained visible as shown by (200) and (220) planes at 2θ ≈ 28.30° and 40.46°, respectively. The intensity ratio of the SnSe (111) peak to the SnTe (200) peak increased significantly to 4.8 and 9.5 at x = 0.6 and 0.8, respectively, suggesting a transition in phase dominance from cubic to orthorhombic. The results suggest a gradual structural transition and phase competition between SnSe and SnTe as the Se/Te ratio varies. Slight shifts in the 2θ positions relative to the standard patterns are due to lattice strain, compositional variations, or synthesis-related factors, which can induce minor distortions while preserving the overall crystal structure.

Table 3 summarises the lattice parameters of the bulk $Sn(Se_xTe_{1-x})$ alloys, with an estimated uncertainty of ± 0.005 Å attributed to peak fitting. The results confirm a distinct structural transition as the Se content increases. At x = 0.0, corresponding to $SnTe_{0.88}$, the material exhibited a cubic crystal structure with lattice parameters $a = b = c = 6.320$ Å, consistent with the values reported in previous studies for cubic SnTe.[11,18–19] However, as the Se content increased to x ≥ 0.6, a phase transition to an

orthorhombic structure was observed, reflected in the anisotropic lattice parameters. For example, the sample with x = 0.6 exhibited orthorhombic lattice parameters of a = 11.680 Å, b = 4.280 Å and c = 4.456 Å. The fully substituted sample (x = 1.0), corresponding to $SnSe_{0.94}$, showed lattice parameters of a = 11.470 Å, b = 4.152 Å and c = 4.439 Å, which are in good agreement with previously reported values for orthorhombic SnSe. [12,14,15,20]

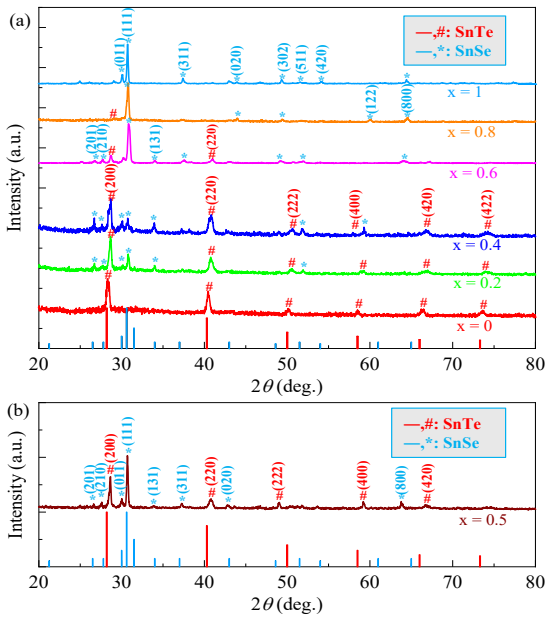

Figure 4: XRD patterns of $Sn(Se_xTe_{1-x})$ bulk alloys with (a) x = 0.0, 0.2, 0.4, 0.6, 0.8, 1.0 and (b) x = 0.5. The vertical bars indicate the standard JCPDS reference peaks for SnTe (No. 46-1210) and SnSe (No. 32-1382).

Table 3: Lattice parameters of $Sn(Se_xTe_{x-1})$ bulk alloys obtained from XRD analysis

No	x	Measured composition	Lattice parameters			
			a (Å)	b (Å)	c (Å)	Type
1	0.0	$SnTe_{0.88}$	6.320	6.320	6.320	Cubic
2	0.2	$Sn(Se_{0.1}Te_{0.8})$	6.310	6.310	6.310	Cubic
3	0.4	$Sn(Se_{0.2}Te_{0.6})$	6.310	6.310	6.310	Cubic
4	0.6	$Sn(Se_{0.52}Te_{0.2})$	11.680	4.280	4.456	Orthorhombic
5	0.8	$Sn(Se_{0.9}Te_{0.1})$	11.510	4.140	4.280	Orthorhombic
6	1.0	$SnSe_{0.94}$	11.470	4.152	4.439	Orthorhombic

The XRD patterns of $Sn(Se_xTe_{1-x})$ thin films with varying Se content (x = 0.0–1.0) exhibited a clear compositional dependence, closely mirroring the structural evolution observed in bulk counterparts (Figure 5). At x = 0.0 (Figure 5[a]), the diffraction peaks appeared at 2θ values of 28.28°, 40.40°, 50.06°, 58.31°, 66.18° and 73.48°, corresponding to the (200), (220), (222), (400), (420) and (422) planes, respectively, which are consistent with the cubic phase of SnTe.[11,18] In contrast, for the thin-film with x = 1.0, the XRD pattern exhibited peaks at 2θ values of 29.50°, 30.48°, 37.86° and 43.62°, indexed to the (011), (111), (311) and (020) planes, respectively, in agreement with the orthorhombic phase of SnSe (Figure 5[f]).[12,14,15,20] For intermediate compositions (x = 0.2–0.8), mixed-phase patterns were evident. At x = 0.2 and 0.4, the diffraction peaks were primarily associated with the cubic SnTe phase, although a weak SnSe (111) reflection appeared at 2θ ≈ 30.48°. The intensity ratio of the SnSe (111) peak to the SnTe (200) peak for x = 0.2 and 0.4 was approximately 0.12 and 0.16, respectively, indicating that the samples were still predominantly cubic. In contrast, at x = 0.6 and 0.8, the orthorhombic SnSe phase became dominant, while weak SnTe reflections corresponding to (200) and (220) planes remained visible at 2θ ≈ 28.28° and 40.40°, respectively. The intensity ratio of the SnSe (111) peak to the SnTe (200) peak increased significantly to 3.5 and 6.5 at x = 0.6 and 0.8, respectively, suggesting a transition in phase dominance from cubic to orthorhombic. These findings demonstrate that the structural trends observed in thin films were consistent with those of the bulk materials, showing a structural transition from the cubic to the orthorhombic phase as the Se content increased. These results suggest that the vacuum evaporation process successfully preserved the essential phase characteristics across the composition range.

The lattice parameters of the $Sn(Se_xTe_{1-x})$ thin films, as listed in Table 4, further support the structural transition indicated by the XRD patterns. Consistent with the trend observed in the bulk materials, increasing Se content induced a phase transformation from a cubic to an orthorhombic structure. At low Se content (x = 0.0), corresponding to ($SnTe_{0.94}$), the thin-film exhibited a cubic crystal characterised by a symmetric lattice ($a = b = c = 6.309$ Å), in agreement with standard cubic SnTe.[17,19] The structure transitioned to an orthorhombic phase with distinct lattice parameters at x ≥ 0.6. For the film with x = 0.6, the lattice constants were determined to be a = 11.660 Å, b = 4.210 Å and c = 4.570 Å. At x = 1.0, the $SnSe_{0.09}$ alloy yielded lattice parameters of a = 11.470 Å, b = 4.152 Å and c = 4.439 Å, confirming the formation of an orthorhombic phase consistent with that of bulk SnSe.[12,13] The phase transition from a cubic structure at x = 0.0 to an orthorhombic structure at x ≥ 0.6, observed in both bulk and thin-film samples, demonstrates the successful structural replication in thin films synthesised from bulk $Sn(Se_xTe_{1-x})$ alloys via vacuum evaporation.

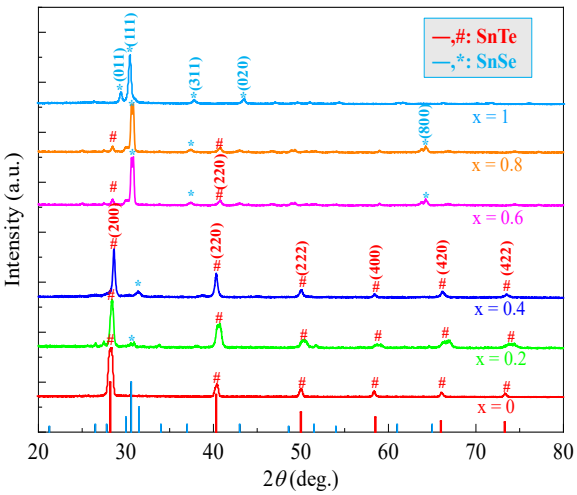

Figure 5: XRD patterns of bulk-derived $Sn(Se_xTe_{1-x})$ thin films. The vertical bars indicate the standard JCPDS reference peaks for SnTe (No. 46-1210) and SnSe (No. 32-1382).

Table 4: Lattice parameters of bulk-derived $Sn(Se_xTe_{x-1})$ thin films obtained from XRD analysis

No	x	Measured composition	Lattice parameters			
			a (Å)	*b* (Å)	*c* (Å)	Type
1	0.0	$SnTe_{0.94}$	6.309	6.309	6.309	Cubic
2	0.2	$Sn(Se_{0.2}Te_{0.7})$	6.310	6.310	6.310	Cubic
3	0.4	$Sn(Se_{0.44}Te_{0.51})$	6.157	6.157	6.157	Cubic
4	0.6	$Sn(Se_{0.55}Te_{0.38})$	11.660	4.210	4.570	Orthorhombic
5	0.8	$Sn(Se_{0.83}Te_{0.18})$	11.420	4.190	4.460	Orthorhombic
6	1.0	$SnSe_{0.94}$	11.470	4.152	4.439	Orthorhombic

The variation in Se within $Sn(Se_xTe_{1-x})$ alloys alters the distribution of interatomic electron bonds, leading to an energy imbalance that stabilises the orthorhombic phase at higher Se concentrations. This process is also influenced by thermodynamic factors, such as changes in formation enthalpy associated with increasing Se content, which ultimately favour the stability of the orthorhombic phase at temperatures suitable for photovoltaic applications.[18,19] The successful preservation of structural integrity during the transition from bulk to thin-film form highlights the importance of precisely controlling the Se content in $Sn(Se_xTe_{1-x})$ alloys to achieve optimal material properties for solar cell applications.

4. CONCLUSIONS

This study systematically investigated the elemental compositions and structural transitions of bulk-derived $Sn(Se_xTe_{1-x})$ thin films. The bulk samples were first synthesised using the Bridgman method, followed by the thin-film fabrication via vacuum evaporation, with Se content varied incrementally (x = 0.0, 0.2, 0.4, 0.6, 0.8 and 1.0). EDX analysis revealed deviations from the ideal stoichiometry in both sample types; however, the thin films exhibited compositions more closely aligned with the intended stoichiometry. SEM images showed that the bulk materials exhibited grain structure variations depending on Se content, while the thin films displayed a more uniform morphology, transitioning from granular to nanostructured patterns as Se content increased. The XRD analysis demonstrated a phase transition from a cubic structure at x = 0.0 to an orthorhombic structure at higher Se concentration ($x \geq 0.6$) in both bulk and thin-film samples, accompanied by variations in lattice parameters, indicating the successful preservation of structural integrity during the transition from bulk to thin-film form. These findings emphasise the importance of precise compositional control during synthesis to achieve the desired stoichiometry and crystal structure of $Sn(Se_xTe_{1-x})$ thin films, thereby enhancing their potential performance for photovoltaic applications.

5. ACKNOWLEDGEMENTS

The authors gratefully acknowledge the Directorate of Research and Community Service, Universitas Negeri Yogyakarta, for funding this research under the Research Group Scheme 2024 (Grant No. B/30/UN34.13/PT.01.07/2024).

6. REFERENCES

1. Ramkumar, M. S. et al. (2022). Semiconductor materials for solar PV technology and challenges towards electrical engineering. *Adv. Mater. Sci. Eng.*, 2022(1), 7272489. https://doi.org/10.1155/2022/7272489
2. Sohail, M. et al. (2024). Recent developments, advances and strategies in heterogeneous photocatalysts for water splitting. *Nanoscale Adv.*, 6(5), 1286–1330. https://doi.org/10.1039/D3NA00442B
3. Ahmad, I. et al. (2023). Semiconductor photocatalysts: A critical review highlighting the various strategies to boost the photocatalytic performances for diverse applications. *Adv. Colloid Interface Sci.*, 311, 102830. https://doi.org/10.1016/j.cis.2022.102830
4. Benda, V. (2020). Photovoltaics, including new technologies (thin film) and a discussion on module efficiency. In Letcher, T. M. (Ed.). *Future energy: improved, sustainable, and clean options for our planet*. Amsterdam: Elsevier, 375–412.

5. Shen, L., Li, Z. & Ma, T. (2020). Analysis of the power loss and quantification of the energy distribution in PV module. *Appl. Energy*, 260, 114333. https://doi.org/10.1016/j.apenergy.2019.114333
6. Raksa, P. et al. (2025). Nanocrystalline lanthanum-doped bismuth ferrite as a perovskite photosensitizer: Morphological, structural, optical, photovoltaic properties, and DFT calculations. *Mater. Lett.*, 386, 138217. https://doi.org/10.1016/j.matlet.2025.138217
7. Hamady, S. O. S. et al. (2019). Development of novel thin film solar cells: Design and numerical optimisation. *J. Phys. Sci.*, 30(2), 199–205. https://doi.org/10.21315/jps2019.30.s2.17
8. Yadav, R. K. et al. (2022). A qualitative study of SnSe thin film solar cells using scaps 1D and comparison with experimental results: A pathway towards 22.69% efficiency. *Sol. Energy Mater. Sol. Cells*, 244, 111835. https://doi.org/10.1016/j.solmat.2022.111835
9. Li, Z. et al. (2020). Effect of film thickness and evaporation rate on co-evaporated SnSe thin films for photovoltaic applications. *RSC Adv.*, 10(28), 16749–16755. https://doi.org/10.1039/D0RA01749C
10. Gu, S. et al. (2017). Self-driven, broadband and ultrafast photovoltaic detectors based on topological crystalline insulator SnTe/Si heterostructures. *J. Mater. Chem. A*, 5(22), 11171–11178. https://doi.org/10.1039/C7TA02222K
11. Feng, D. et al. (2017). Hydrothermal synthesis of SnQ (Q = Te, Se, S) and their thermoelectric properties. *Nanotechnol.*, 28(45), 455707. http://doi.org/10.1088/1361-6528/aa8b29
12. Shi, W. et al. (2018). Tin selenide (SnSe): Growth, properties, and applications. *Adv. Sci.*, 5(4), 1700602. https://doi.org/10.1002/advs.201700602
13. Patel, K. et al. (2020). Orthorhombic SnSe nanocrystals for visible-light photodetectors. *ACS Appl. Nano Mater.*, 3(11), 11143–11151. https://doi.org/10.1021/acsanm.0c02301
14. Jagani, H. S. et al. (2022). Self-powered anisotropic photo-responsive properties of tin mono-selenide (SnSe) photodetector. *Opt. Mater.*, 132, 112756. https://doi.org/10.1016/j.optmat.2022.112756
15. Patel, K. et al. (2024). X-ray diffraction analysis of orthorhombic SnSe nanoparticles by Williamson–hall, Halder–Wagner and size–strain plot methods. *Chem. Phys. Impact*, 8, 100547. https://doi.org/10.1016/j.chphi.2024.100547
16. Ariswan, A., Prasetyowati, R. & Sutrisno, H. (2018). Physicochemical properties of $Sn(S_x,Te_{1-x})$ solid solutions of both massive materials and thin films. *Chalcogenide Lett.*, 15(3), 173–180.
17. Jamwal, G. et al. (2023). Structural, electronic and thermoelectric properties of SnTe with dilute co-doping of Ag and Cu. *J. Alloys Compd.*, 954, 170182. https://doi.org/10.1016/j.jallcom.2023.170182
18. Mandal, P. et al. (2020). Visible-light active electrochemically deposited tin selenide thin films: synthesis, characterization and photocatalytic activity. *J. Mater. Sci.: Mater. Electron.*, 31, 4708–4718. https://doi.org/10.1007/s10854-020-03027-0
19. Li, W. et al. (2014). Non-monotonic pressure dependence of band gap in SnTe. *Chem. Phys. Lett.*, 616, 196–198. https://doi.org/10.1016/j.cplett.2014.10.050

20. Ariswan, Sutrisno, H. & Prasetyawati, R. (2017). Crystal structure, optical, and electrical properties of SnSe and SnS semiconductor thin films prepared by vacuum evaporation techniques for solar cell applications. In *IOP Conference Series: Materials Science and Engineering* (012042). https:/doi.org/10.1088/1757-899X/202/1/012042
21. Tan, C. et al. (2020). Evaporated Se_xTe_{1-x} thin films with tunable bandgaps for short-wave infrared photodetectors. *Adv. Mater.*, 32(38), 2001329. https://doi.org/10.1002/adma.202001329
22. Ghazala, M. S. A. et al. (2020). Fabrication of nanocrystalline silicon thin films utilized for optoelectronic devices prepared by thermal vacuum evaporation. *ACS Omega*, 5(42), 27633−27644. https://doi.org/10.1021/acsomega.0c04206
23. Christy, D. S., Sahaya, S. X. & Mahadevan, C. K. (2022). Study of physico-chemical properties and growth dimension augmentation of barium succinate single crystals grown by slow evaporation technique. *J. Phys. Sci.*, 33(1), 24−29. https://doi.org/10.21315/jps2022.33.1.3
24. Fernandes, P. A. et al. (2013). Thermodynamic pathway for the formation of SnSe and $SnSe_2$ polycrystalline thin films by selenization of metal precursors. *Cryst. Eng. Comm.*, 15(47), 10278−10286. https://doi.org/10.1039/C3CE41537F